CHEMSUSCHEM

ChemPubSoc Europe

DOI: 10.1002/cssc.201200450

Crystallinity-Controlled Titanium Oxide–Carbon Nanocomposites with Enhanced Lithium Storage Performance

Yuanyuan Zhou,[a] Jinwoo Lee,[b] Chul Wee Lee,[a] Mihye Wu,[a] and Songhun Yoon*[a]

Nanocomposites of crystalline-controlled TiO_2–carbon are prepared by a novel one-step approach and applied in anodes of lithium ion batteries. In our nanocomposite anodes, the Li^+ capacity contribution from the TiO_2 phase was enormous, above 400 mAh g^{-1} ($Li_{1+x}TiO_2$, $x>0.2$), and the volumetric capacity was as high as 877 mAh cm^{-3} with full voltage utilization to 0 V versus Li/Li^+, which resulted in higher energy density than that of state-of-the-art titania anodes. For the first time, it was clearly revealed that the capacity at 1.2 and 2.0 V corresponded to Li^+ storage at amorphous and crystalline TiO_2, respectively. Furthermore, improvements in the rate capability and cycle performance were observed; this was attributed to resistance reduction induced by higher electrical/Li^+ conduction and faster Li^+ diffusion.

Introduction

Tremendous efforts have been made to develop advanced anode materials for lithium ion batteries (LIBs). In particular, nanoporous transition-metal oxides, such as TiO_2,[1–3] MoO_2,[4] Fe_2O_3,[5] CoO,[6] and WO_{3-x},[7] have been intensively investigated as promising anode candidates for LIBs due to their characteristic properties, such as high Li^+ diffusion within the nanosized pore wall, improved electrolyte penetration through well-interconnected pores, and better availability of charge-storage sites from its high surface area.[1–9] Nanostructured TiO_2 polymorphs (anatase nanotube, rutile nanoparticle, and TiO_2-B nanowires, etc.) have been applied as anodes in LIBs because of their properties, such as low cost, low toxicity, and easy formation of nanostructures.[10–13] In particular, the anatase TiO_2 nanotube electrode showed improved rate performance due to the characteristic nanosized tubular morphology.[10] In the case of rutile TiO_2 nanoparticles, high Li^+ uptake (0.6 Li^+ per TiO_2) was observed, whereas the bulk rutile TiO_2 electrode was electrochemically inactive.[11] Similarly, it was reported that 0.8 Li^+ could be stored within TiO_2-B nanowires.[12–13] Despite the reported advanced performance of nanostructured TiO_2 anodes, several intrinsic shortcomings, such as low discharge capacity below 250 mAh g^{-1} and insufficient electrical conductivity, are inevitable. Consequently, the energy density and power capability of TiO_2 anodes are limited, which hinders the practical application of TiO_2 anodes in high-power/-energy devices, such as hybrid electric vehicles (HEVs) and electric vehicles (EVs). To overcome these obstacles, enhancement in capacity and electrical conductivity are crucial for the advancement of TiO_2-based anodes.

In our previous report, an ordered mesoporous carbon–silica–titania material was prepared by using the novel tetra-constituent co-assembly (tetra-CCA) method.[8] The nanocomposite anode prepared exhibited high capacity, high initial efficiency, and improved rate performance from 2.5 to 0 V versus Li/Li^+. It remains unclear why such performance improvement was observed and how nanosized silica and titania phases could influence anode performance. It was reported that amorphous TiO_2 (A-TiO_2) anode materials prepared after low-temperature heat treatment (127 °C)[14] exhibited high discharge capacity (335 mAh g^{-1}, 1 Li^+ uptake; formation of $LiTiO_2$) and sloped discharge patterns from 2.5 to 0.8 V versus Li/Li^+ were observed. On the contrary, poor initial efficiency (40–50 %) was commonly observed, which could be much worse once the low cutoff voltage was extended to 0 V versus Li/Li^+. This undesirable coulombic efficiency was attributed to high electrolyte reactivity with detrimental functional groups or species on TiO_2 surfaces and a less-developed crystal structure resulting from the low-temperature heat treatment.[14,15] Also, relatively poor cyclability was observed because the titania structure was unstable as a result of the low-temperature heat treatment. To improve the initial efficiency and cyclability, a high calcination temperature (above 300 °C) becomes indispensable and generally promotes titania crystallization accompanied by a capacity decrease and voltage plateau formation.[10] Therefore, control of the crystallization of titania at high temperatures will be crucial to develop a high-capacity titania anode with high initial efficiency. Furthermore, improvement of the rate capability can be achieved by preparing nanocomposites

[a] Y. Zhou, Dr. C. W. Lee, M. Wu, Dr. S. Yoon
Green Chemical Technology Division
Korea Research Institute of Chemical Technology (KRICT)&
University of Science and Technology (UST)
Daejeon 305-600 (Korea)
Fax: (+82) 42-860-7389
E-mail: yoonshun@krict.re.kr

[b] Dr. J. Lee
Department of Chemical Engineering
Pohang University of Science and Technology
Kyungbuk 790-784 (Korea)

Supporting Information for this article is available on the WWW under http://dx.doi.org/10.1002/cssc.201200450.

of TiO_2 with electrically conductive carbon material.[16,17] As a typical example, TiO_2(B)@carbon nanowires were prepared and applied in an anode within the voltage range from 0 to 3 V.[18] Characteristic Li^+ storage peaks were observed near 1.5 V, indicating that Li^+ uptake dominantly happened at crystalline TiO_2(B) phase. Despite the high discharge capacity and stable cycle life, the observed rate capability remained below 50% retention at 0.5 C and also the initial efficiency was as low as 52%. Regardless of the high rate capability of film-type A-TiO_2 electrodes prepared by evaporative vapor deposition, very low material loading due to a fundamental thickness limit below sub-μm levels make such electrodes far from practical.[15] Several reports of promising approaches to advance the rate performance of titania anodes by dispersion of nanosized titania into a conductive mesoporous carbon skeleton, based on simple physical mixing or contact between carbon and titania, have appeared in the literature.[8,34,36]

Results and Discussion

Herein, we present a novel preparative method for complete nanocomposites of A-TiO_2 carbon in one-step, high-temperature calcination. In addition, the crystallinity of TiO_2 was controlled by changing the titania precursors. For this purpose, titanium citrate complex (TiCA) and a titanium acid–base pair (TiAB) are utilized as titanium precursors, which are then converted into the A-TiO_2[8,19] and crystalline (C-TiO_2) phases[20–23] embedded in the carbon phase after calcination in an inert atmosphere, respectively. The lithium storage performance of the nanocomposite electrodes prepared was investigated to clarify the influence of TiO_2 crystallinity on capacity. Because the amorphous state of TiO_2 is preserved after high-temperature calcination, a high capacity, improved initial efficiency, and stable cyclability are expected. To the best of our knowledge, the relationship between TiO_2 crystallinity and Li^+ storage properties is revealed for the first time.

The overall preparation is schematically shown in Figure 1. In this approach, the tetra-CCA method was utilized for the purpose of a one-step preparation of ordered mesoporous TiO_2/carbon nanocomposites with controlled TiO_2 crystallinity. PF resol and P123 surfactant were added as the carbon precursor and pore-forming agent, respectively. TiAB, which has typically been used for the formation of ordered an structure by self-assembly, was preliminary reacted and then converted to the C-TiO_2 phase after high-temperature calcination.[17–21] TiCA, which has a cage-like molecule with epitaxial hydroxyl groups, can strongly interact with resol molecules by hydrogen bonding and the formation of a cross-linked structure within the polymer matrix through a Pechini-like reaction during a subsequent curing process.[8,17,35] Due to strong confinement of rigid polymers, the amorphous titania nanophase was preserved even after the final high-temperature calcination at 600 °C.[8,17,35] Compared with TiAB, phase separation after curing barely occurred between TiO_2 and the polymer in the case of the TiCA precursor; this was attributed to the likely formation of hybrid polymer between TiCA and resols. This assumption has been supported by the reported work by Zhao et al.[19,21] and our previous work.[8,34] Herein, the molar ratio between TiCA and TiAB was varied for the purpose of controlling the TiO_2 crystallinity. In our approach, four constituents of PF resol, TiAB, TiCA, and P123 produced novel ordered mesoporous TiO_2–carbon nanocomposites by evaporation-induced self-assembly (EISA) and subsequent heat treatment. A calcination temperature of 600 °C was selected because functional groups on the surface of carbon and titania could be completely removed, while collapse of the mesostructure due to TiO_2 crystal growth could be minimized.[21,23] To the best of our knowledge, this is the first report on the preparation of ordered mesoporous TiO_2–carbon nanocomposite (MACT) materials with controlled TiO_2 crystallinity. The molar ratio (A/C) of TiCA and TiAB was varied from 1:3 (MACT1) to 1:1 (MACT2) and 3:1 (MACT3). As listed in Table 1, the estimated weight fraction of each component (A-TiO_2, C-TiO_2, and carbon) of the MACT materials was based on total the Ti elemental fraction obtained by inductively coupled plasma (ICP) analysis.

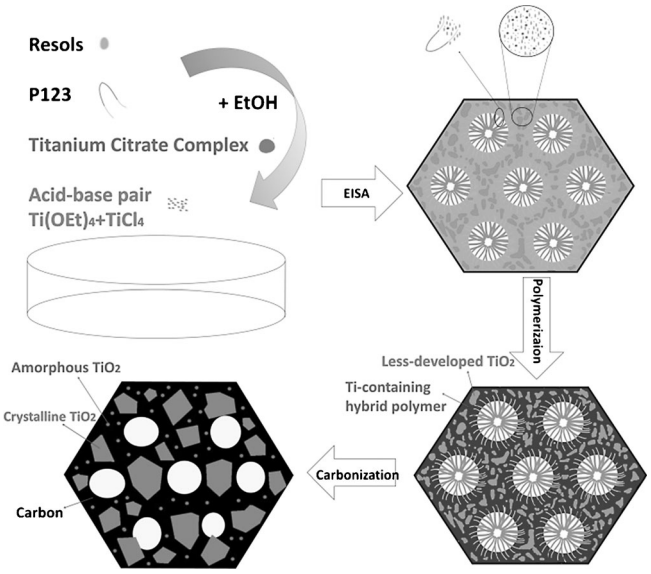

Figure 1. Schematic description of the formation mechanism of MACT materials. Here, PF resol and P123 are the carbon precursor and surfactant, respectively. Note that TiCA and acid–base pair of titanium source are converted into the amorphous and the C-TiO_2 phase.

The small- and wide-angle XRD patterns for MACT1, MACT2, and MACT3 are shown in Figure 2. In the small-angle XRD patterns, a broad peak associated with pore ordering was observed at around $2\theta = 1^\circ$ for every MACT material, indicating that an ordered structure was maintained despite the presence of a large amount of TiO_2 (above 50 wt%).[21] Close examination of the XRD patterns revealed that the peak gradually shifted to higher 2θ values with an increasing A/C ratio; this was indicative of the smaller lattice parameter resulting from the more amorphous structure.[37] In the wide-angle XRD patterns, the peaks corresponding to the anatase TiO_2 phase (denoted in parentheses) and a broad carbon peak located near $2\theta = 25^\circ$ were commonly observed for the MACTs.[16] Interestingly, the peak intensity of anatase TiO_2 became smaller as the A/C ratio increased to reflect the reduction in anatase TiO_2 crystallinity

Table 1. Changes in the physical properties and anode performance of MACT materials.

Material	Fraction[a] [wt%] A-TiO_2	C-TiO_2	carbon	Ratio A-TiO_2/C-TiO_2[b]	S_{TiO_2}[c] [nm]	A_{BET}[d] [$m^2 g^{-1}$]	C_{dis} [$mAh g^{-1}$]	IE[e] [%]	Rate capability[f] [%]	Discharge retention[g] [%]
MACT1	14.9	44.7	40.3	1:3	6	132	289	51	47	64
MACT2	28.4	28.4	43.3	1:1	5	85	350	53	48	72
MACT3	39.9	13.3	46.8	3:1	4	72	430	66	56	78

[a] The fractions of TiO_2 and C were obtained by ICP methods and the fractions of A-TiO_2 and C-TiO_2 were estimated from the expected molar ratio of A-TiO_2 to C-TiO_2. [b] The molar ratio of A-TiO_2 to C-TiO_2 obtained from adding the molar amounts of TiCA and TiAB. [c] The crystal size of TiO_2 was estimated from the FWHM of the X-ray diffraction (XRD) peak. [d] The BET surface area (A_{BET}) was obtained by Ar sorption analysis. [e] The initial discharging capacity (C_{dis}) and initial efficiency (IE) were obtained from galvanostatic charge–discharge experiments. [f] The rate capability was obtained by dividing the discharge capacities at rates of 0.2 and 2 C. [g] The cycle performance was estimated by the discharge capacity retention after the 40th cycle at 0.1 C.

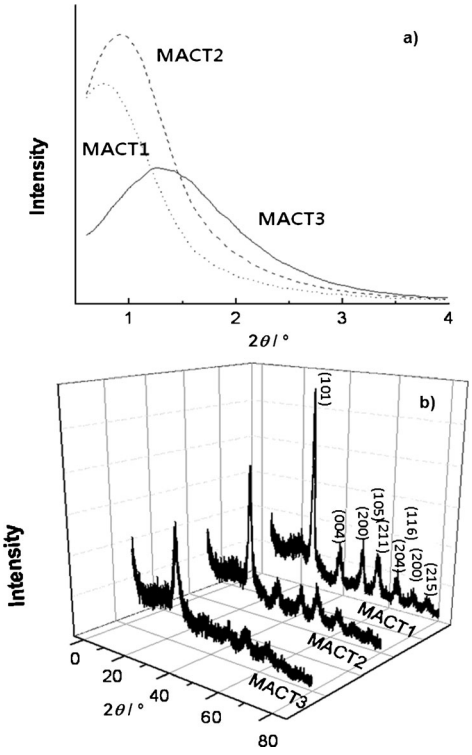

Figure 2. Small-angle X-ray scattering patterns (a) and wide-angle XRD patterns (b) of the MACT materials.

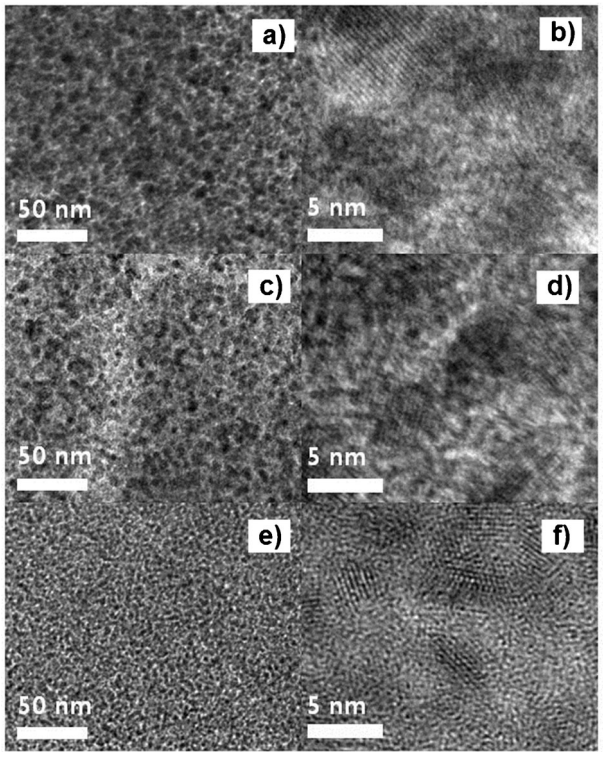

Figure 3. TEM images of MACT1 (a and b), MACT2 (c and d), and MACT3 (e and f).

and increase in the amorphous phase. The average crystal size was calculated from the full-width at half-maximum (FWHM) of the anatase peaks at 35° by using the Scherrer equation (Table 1) and showed that the average crystal size increased from 4 to 6 nm as the A/C ratio increased.[38]

TEM images of the MACT materials are shown in Figure 3 and Figure S1 in the Supporting Information. As can be seen, wormhole-like mesopores appeared in all MACT samples and nanosized TiO_2 crystals were homogeneously distributed. As the TiCA concentration increased, the size of the TiO_2 nanocrystals became smaller, coinciding with the change in crystal size determined by XRD peak analysis (Table 1). The TEM images also indicated that a decrease in the lattice parameter from MACT1 to MACT3 could be easily identified, although the ordered mesostructure was not clear for MACTs; this was in good agreement with peak shifting observed in the small-angle XRD patterns. To confirm uniform dispersion of TiO_2 in the MACT materials, energy-dispersive X-ray (EDX) analysis in point and area mode was conducted on MACT1 as a representative material and showed that carbon, titanium, and oxygen were homogeneously located within the nanocomposite (Figure S2 in the Supporting Information). The TiO_2 nanocrystals were probably surrounded by carbon and the A-TiO_2 phase, in agreement with our previous result.[8] Furthermore, the XPS spectrum for Ti2p in MACT1 (Figure S3 in the Supporting Information) was selected to verify the oxidation state of Ti. Two symmetric Ti 2p peaks at 458.9 and 464.6 eV, similar to pure TiO_2, were observed and indicated stoichiometric TiO_2 with a low concentration of defects.[24] Figure S4 in the Supporting Information shows the Ar sorption isotherms and pore size dis-

tributions (PSDs) for the MACT materials. The Ar adsorption volume became smaller as the A/C ratio increased. This volume decrease was attributed to the higher fraction of TiO_2. From the PSDs of the MACTs, MACT exhibited a main pore size of 2 nm, which coincided with the TEM shown in Figure 3. Considering that the lattice parameter decreases and the pore size is constant, the pore wall thickness is expected to be smaller as the A/C ratio increases. Note that the amount of micropores below 2 nm gradually reduced as A-TiO_2 increased, which implied a gradual loss of microporosity for the MACTs. The loss of microporosity was the main cause for the decrease in the measured BET surface area from MACT1 to MACT3 (Table 1).

Figure 4 shows the galvanostatic charge–discharge patterns and their differential capacitance profiles of MACT electrodes under a 0.1 C current rate in the voltage range from 2.5 to 0 V

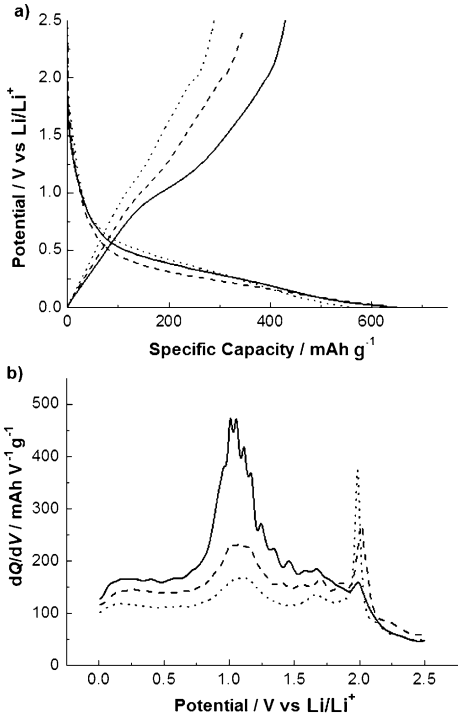

Figure 4. a) Initial galvanostatic charge–discharge patterns and b) the differential capacity plots of the MACT3 (——), MACT2 (- - - -), and MACT1 (•••••) electrodes at 0.1 C rate in the voltage range from 0 to 2.5 V versus Li/Li^+.

versus Li/Li^+. It is well known that conventional nanostructured TiO_2 or its nanocomposites with carbon utilizes a narrow voltage range from 2.5 to 1.0 V because the Li^+ addition reaction into TiO_2 mostly occurs near 1.5 V as a voltage plateau. Below 1 V, the undesirable irreversible reaction of H_2O/OH species to Li_2O and/or an electrolyte decomposition reaction on carbon surface occur.[14,25] Because A-TiO_2 in our MACT materials survives even after high-temperature calcination, it is expected that the Li^+ addition reaction can extend below 1 V with retarded irreversible surface reactions. As shown in Figure 4, the specific charge and discharge capacity becomes larger as A-TiO_2 increases. In particular, the MACT3 electrode showed a high specific discharge capacity (C_{dis}) of 430 mAh g^{-1} and an improved initial efficiency (IE) of 66% (Table 1). When the mesoporous carbon materials prepared by EISA using a triblock copolymer surfactant template are applied in anodes, the Li^+ storage capacity is known to be proportional to the surface area and pore structures.[25,39] Typically, a diconstituent ordered mesoporous carbon (di-OMC) electrode prepared by a very similar method to our MACT materials was reported to have surface area of 650 $m^2 g^{-1}$, a discharge capacity C_{dis} of about 300 mAh g^{-1}, and a low IE of 30%.[25] Hence, the capacity contribution of the carbon framework in MACT3 is estimated to be lower than 200 mAh g^{-1} when considering a carbon fraction of 47 wt% and lower surface area of the MACT materials. Therefore, the Li^+ uptake contribution in MACT3 of TiO_2 itself was as high as above 400 mAh g^{-1}, which corresponded to 1.2 Li^+ uptake within the TiO_2 phase ($Li_{1+x}TiO_2$, $x > 0.2$). Typically, the highly crystalline nanostructure of TiO_2 polymorphs have exhibited reversible discharge capacity as low as about 250 mAh g^{-1} ($Li_{0.6}TiO_2$) after high-temperature calcination above 300 °C. In spite of the high discharge capacity of 335 mAh g^{-1} (Li_1TiO_2) in A-TiO_2 anodes, very low IE and poor cycle performance were inevitable due to the low heat-treatment temperature near 100 °C, which increased irreversible reactions of H_2O/OH species on the TiO_2 surface to Li_2O.[1,14] In the literature, it was reported that an A-TiO_2 film from evaporative vapor deposition at 80 °C exhibited a high initial efficiency of 63% within the voltage range from 1 to 3 V versus Li/Li^+.[15] However, it is reasonable that the irreversible surface reactions during the first cycle can be aggravated if the low cutoff voltage is extended to 0 V versus Li/Li^+ in the low-temperature-treated A-TiO_2 electrodes, which can result in much smaller IE than our MACT electrodes. To the best of our knowledge, the electrode composed of MACT3 accommodated the highest Li^+ storage within the TiO_2 phase above 1.2 Li^+ uptake, while maintaining a high IE, which was mostly ascribed to survival of the nanosized A-TiO_2 phase embedded within a highly conductive carbon skeleton, even after high-temperature carbonization at 600 °C. In addition, the volumetric capacity of the MACT3 material was as high as 877 mAh cm^{-3}, which was much higher than the conventional carbon-based anode (< 600 mAh cm^{-3}).[26,27] When compared with the energy density of a typical C-TiO_2 anode (0.6 kWh kg^{-1}), the MACT3 electrode can deliver a much higher energy density of 1.5 kWh kg^{-1}, which is comparable to high-energy graphite anodes (1.4 kWh kg^{-1}).[28]

As shown in Figure 4a, the voltage patterns during charging (downward direction) remained similar; this was associated with Li^+ addition. In contrast, we observed an interesting change during discharging related to Li^+ extraction (upward direction). The discharge capacity associated with a sloped region near 1 V increased, but a narrow voltage plateau at 2.0 V vanished as A-TiO_2 increased. From the differential capacity plots shown in Figure 4b, the individual capacity contribution by the A-TiO_2 and C-TiO_2 phases was considered separately. For every MACT electrode, two peaks located at 1.2 and 2.0 V were commonly observed. In the literature, it has been reported that the crystalline anatase phase showed a character-

istic plateau near 1.8 V, which indicated that the peak at 2.0 V in Figure 4b corresponded to Li^+ extraction from the C-TiO_2.[10–13] As the weight fraction of A-TiO_2 increased, the peak intensity at 2.0 V decreased, but an increase in the peak intensity at 1.2 V was observed, which was associated with the decrease of crystallinity observed in the XRD patterns shown in Figure 2b. This contradictory trend of these two peaks revealed that the capacity near 1.2 V was relevant to Li^+ extraction from the A-TiO_2 phase. Importantly, an increase in the peak area at 1.2 V was more distinct than that at 2.0 V, which was certainly relevant to higher Li^+ uptake per Ti in A-TiO_2 than C-TiO_2. Our observation is the first report to demonstrate the individual influence of the A and C phases in TiO_2 on the anode capacity contribution. When one uses A-TiO_2 prepared by low-temperature treatment, however, it is expected that the observation of lithium uptake at 1.2 V is difficult due to increased irreversible reactions of surface functional groups with the electrolyte.[15,16] Also, note that carbon itself can make an overall contribution to the differential capacity plots due to its discharge pattern indicated by the line with an almost constant slope.[23]

To evaluate the rate capability, galvanostatic charge–discharge testing was conducted at a different current rate from 0.2 to 2 C and capacity retention was plotted against the rate of C, as shown in Figure 5b. As seen, a slightly higher rate capability was observed for the MACT3 electrode (56% retention at a 2 C rate). The change of charge–discharge profiles are shown in Figure S5 in the Supporting Information. For the MACT3 electrode, the initial *IR* drop after potential switching from charge to discharge changed slightly, which was indicative of low polarization resistance. For the rate capability of the TiO_2(B)@carbon composite nanowire anode, about 50% capacity retention was estimated under a current rate of 300 mA g^{-1}, which was smaller than that of MACT3 electrode (70% retention) at the same current density. This improvement is possibly attributed to faster Li^+ transport in A-TiO_2 and higher electrical conductivity when prepared at a higher carbonization temperature than that of the C-TiO_2(B)@carbon electrode.[18] Moreover, thinner active-material pore walls and smaller C-TiO_2 crystals of MACT3, which resulted in a shorter Li^+ diffusion length, were beneficial for the rate performance. Figure 5a shows the cycle performance of the three electrodes, measured at 0.1 C for 40 cycles from 0 to 2.5 V versus Li/Li^+. For all electrodes, the capacity decreased until the third cycle and then stable cycle performance was observed. The initial capacity decay was similar to the reported gradual capacity decay in di-OMC electrodes, indicative of the influence of the carbon skeleton on cycle performance in MACT electrodes.[25] However, the MACT electrodes showed better cycle performance than the di-OMC electrode (65% retention after 40 cycles).[23] This improved cycle performance was probably due to the stable TiO_2 phase within the nanocomposites. The MACT3 electrode showed advanced cycle performance compared with the other two electrodes (Table 1); this may be associated with a more homogenous composite structure with less phase separation between TiO_2 and carbon and less volume expansion in less crystalline TiO_2.[8] In addition, the change of coulombic efficiency according to cycle number was plotted (Figure S6 in the Supporting Information). Despite the intrinsic variation of efficiency characteristic in TiO_2 anode materials, the overall efficiency was maintained above 99%, which was indicative of the high possibility of practical applications.

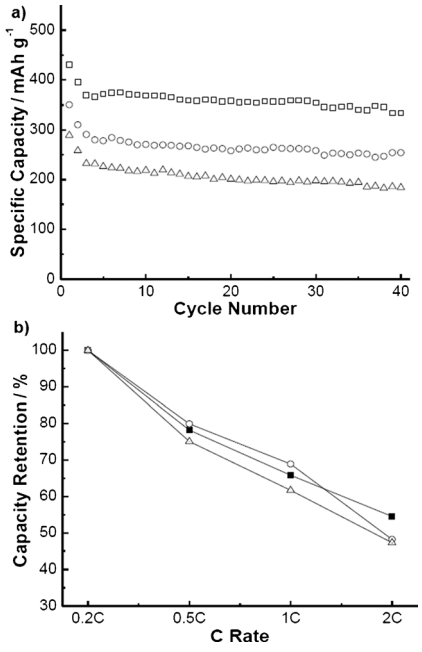

Figure 5. a) Cycle performance of the MACT3 (■), MACT2 (○), and MACT1 (△)electrodes at a current rate of 0.1 C. b) Rate capability results of the MACT3 (□), MACT2 (○), and MACT1 (△) electrodes for current rates from 0.2 to 2 C.

For the purpose of detailed analysis of the resistance change, electrochemical impedance spectroscopy (EIS) was carried out for the MACT2 and MACT3 electrodes in the 5×10^{-3} to 10^5 Hz frequency region in the fully lithiated state (0 V), the A-TiO_2 active state (1 V), and the C-TiO_2 active state (2 V). Figure 6 displays the EIS spectra in the form of Nyquist plots. In general, the EIS spectra were composed of one or two semicircles in the high-frequency region followed by a straight line, according to frequency decrease; this has been frequently observed in anodes for an LIB.[29,34] It has been reported that the resistance from the distributed semicircle (R_{semi}) can include overall electrical/Li^+ conduction within the electrode and ionic transport within the surface film.[29,30,34] With the decrease in frequency, resistance corresponding to the charge-transfer reaction at the interface (R_{ct}) and the Warburg diffusion process, expressed as a straight line, appear.[17,29–32] In the fully lithiated state (0 V), R_{semi}, R_{ct}, and Warburg diffusion were clearly observed for both electrodes. In the A-TiO_2 active state (1 V), interestingly, the value of R_{semi} for MACT3 was reduced, whereas that of MACT2 increased. This decrease of R_{semi} in the MACT3 electrode can probably be ascribed to higher electrical/Li^+ conduction due to a large increase in the differential capacity peak at 1.2 V, which is similar to changes in the EIS spectra during deep charging in the graphite anode.[19,30] Moreover, an increase in diffusion resistance was commonly observed for both electrodes due to delithiation within the electrodes as the measuring voltage increased. After increasing the potential

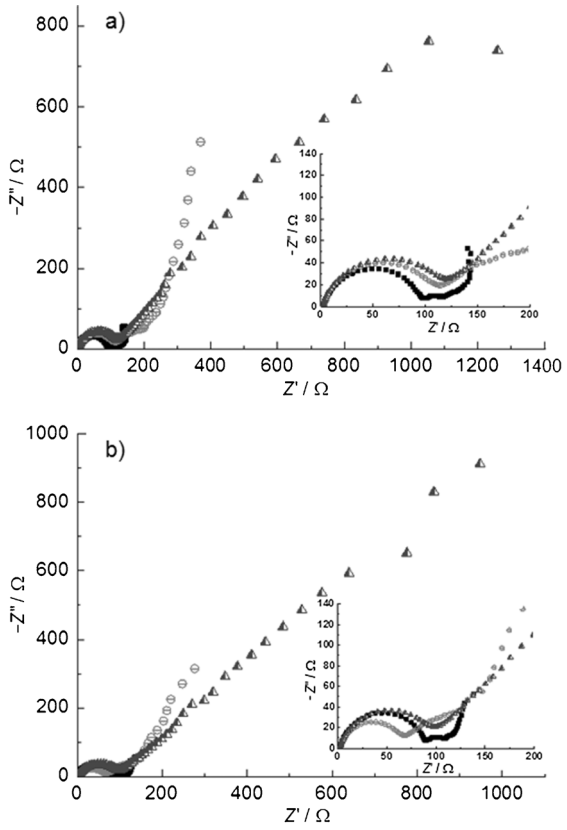

Figure 6. EIS spectra expressed as Nyquist plots with a change of measuring potential for MACT2 (a) and MACT3 (b) at 0 (■), 1 (○), and 2 V (▲).

to 2 V, both electrodes exhibited an increase in R_{semi}, which was attributed to Li^+ extraction in the C-TiO_2 phase.[32] Note that the overall resistance of MACT3 remained smaller than that of the MACT2 electrode, which resulted in a higher rate capability in the MACT3 electrode, as shown in Figure 5b. When compared with pure C-TiO_2 anodes reported in the literature, the relatively low rate capability of the MACT electrodes was due to intrinsically slow Li^+ diffusion within the low-crystalline carbon phase (D_{Li^+}: 10^{-12}–10^{-15} $cm^2 s^{-1}$), which was much smaller than that in the TiO_2 phase (D_{Li^+}: 10^{-8}–10^{-9} $cm^2 s^{-1}$).[32,33] This tendency coincided with the anode of the TiO_2(B)@carbon composite nanowires, which exhibited an abrupt decrease of rate capability due to the full utilization of carbon capacity caused by lowering the cutoff voltage to 0 V.[18] Note that the rate capability of MACT electrodes was better than conventional carbon-based anode materials.[25,30]

Conclusions

MACT materials demonstrated a high specific/volumetric capacity, a high initial efficiency, good rate capability, and high cyclability due to highly capacitive Li^+ uptake in the A-TiO_2 phase, which survived even after high-temperature heat treatment. In addition, the low preparation cost and improved stability of MACT materials will promote their practical use as superior LIB anodes with high energy density and power capability.

Experimental Section

Preparation of MACT materials: The resols (MW < 500) and TiCA were prepared according to literature procedures.[8,15] The prepared resol (20 wt%) and TiCA (0.5 M) were dissolved in ethanol for direct use. In a typical preparation of MACT material, P123 (1 g; PEO-PPO-PEO, Aldrich) was dissolved in ethanol (20 g). $TiCl_4$ (4.8 mmol; Aldrich), $Ti(OEt)_4$ (2.7 mmol; Aldrich), and 0.5 M TiCA solution (5 mL) were sequentially added dropwise under vigorous stirring. Then, 20 wt% resol solution (1.5 g) was added dropwise and the solution immediately changed to orange. After stirring for 2 h, the solution was poured into a big dish and kept in an ambient environment until a glue-like film formed. Then the dish was heated in an oven at 100 °C in air for 24 h until a transparent orange polymeric film was acquired. The film was peeled off the dish, roughly ground, and then carbonized at 450 °C for 2 h and 600 °C under a nitrogen flow in a furnace for 2 h (the ramping rate was 2 °C min^{-1} before 450 °C and 5 °C min^{-1} after 450 °C). After cooling to room temperature, the resulting black product was collected and further ground into a fine powder for subsequent experimental use. The sample was indexed as MACT1 (the color change during a typical preparation procedure was recorded and is shown in Figure S7 in the Supporting Information). MACT2 and MACT3 were prepared following a similar procedure, simply by adjusting the adding molar ratio of $TiCl_4$, $Ti(OEt)_4$, and TiCA, while keeping the total amount of Ti constant ($TiCl_4$/$Ti(OEt)_4$/TiCA = 3.2:1.8:5.0 for MACT2, $TiCl_4$/$Ti(OEt)_4$/TiCA = 1.6:0.9:7.5 for MACT3).

Material characterization: Images of the materials were recorded by using a transmission electron microscope (JEOL JEM-2010). EDX analysis was conducted in the point and area modes by using a co-equipped EDX analyzer attached to the TEM apparatus. The XRD patterns were obtained with a Rigaku D/Max-3C diffractometer equipped with a rotating anode and $Cu_{K\alpha}$ radiation (λ = 0.15418 nm). Aluminum and glass substrates were used for the small- (2θ = 0.6–5°) and wide-angle (2θ = 5–85°) XRD measurements, respectively. The pore size distribution (PSD) was analyzed by using an Ar adsorption measurement (Micrometrics ASAP 2010); the sample for measurement was pretreated at 150 °C for 2 h under vacuum. X-ray photoelectron spectroscopy (XPS) experiments were carried out in ultrahigh vacuum by using a Scienta ESCA-300 high-resolution X-ray photoelectron spectrometer. The Ti elemental fraction was determined by inductively coupled plasma (ICP) mass spectrometry using an Agilent 7700x instrument.

Electrochemical performance investigation: For the preparation of composite anodes, MACT powders were mixed with a conducting agent (Super P) and polyvinylidene difluoride (PVDF) binder with a weight ratio of 8:1:1. The mixture was then dispersed in *N*-methylpyrrolidone (NMP) and spread on Cu foil (apparent areas of 1 cm^2), followed by pressing and drying at 120 °C for 12 h. The half-cell characteristics were analyzed with a coin-type (CR2016) two-electrode cell in which lithium foil (Cyprus Co.) was used. The electrolyte was 1.0 M $LiPF_6$ in 1:1 (*v*/*v*) ethylene carbonate (EC)/dimethyl carbonate (DMC) (Tomiyama Co.). To investigate the anode performance in a LIB, galvanostatic charge–discharge testing in a voltage range of 2.5 to 0 V versus Li/Li^+ was conducted. For the rate performance measurement, the current was varied from 0.1 to 2 C. The cycle performance for 40 cycles was recorded at a 0.1 C rate. All of the electrochemical measurements were made by using a WBCS-3000 battery cycler (WonATech Co.) at ambient temperature in a glove box filled with argon. For AC impedance measurements, a frequency range of 10^6 Hz–5 mHz was used with an AC amplitude of 10 mV (Ivium potentiostat).

Acknowledgements

This work was financially supported by institutional support from the Korea Research Institute of Chemical Technology (KRICT) funded by the Ministry of Knowledge Economy (MKE), Republic of Korea.

Keywords: crystallinity · electrochemistry · lithium · nanostructures · titanium

[1] D. Wang, D. Choi, Z. Yang, V. V. Viswanathan, Z. Nie, C. Wang, Y. Song, J.-G. Zhang, J. Liu, *Chem. Mater.* **2008**, *20*, 3435.
[2] W. Yue, X. Xu, J. T. S. Irvine, P. S. Attidekou, C. Liu, H. He, D. Zhao, W. Zhou, *Chem. Mater.* **2009**, *21*, 2540.
[3] J. J. Fu, T. Zhang, Q. Cao, H. P. Zhang, Y. P. Wu, *Electrochem. Commun.* **2007**, *9*, 2140.
[4] Y. Shi, B. Guo, S. A. Corr, Y.-S. Hu, K. R. Heier, L. Chen, R. Seshadri, G. D. Stucky, *Nano Lett.* **2009**, *9*, 4215.
[5] B. Sun, J. Horvat, H. S. Kim, W.-S. Kim, J. Ahn, G. Wang, *J. Phys. Chem. C* **2010**, *114*, 18753.
[6] P. Poizot, S. Laruelle, S. Grugeon, L. Dupont, J.-M. Tarascon, *Nature* **2000**, *407*, 496.
[7] S. Yoon, C. Jo, S. Y. Noh, C. W. Lee, J. H. Song, J. Lee, *Phys. Chem. Chem. Phys.* **2011**, *13*, 11060.
[8] Y. Zhou, Y. Kim, C. Jo, J. Lee, C. W. Lee, S. Yoon, *Chem. Commun.* **2011**, *47*, 4944.
[9] Y. Zhou, C. W. Lee, S. Yoon, *Electrochem. Solid-State Lett.* **2011**, *14*, A157.
[10] J. Kim, J. Cho, *J. Electrochem. Soc.* **2007**, *154*, A542.
[11] Y.-S. Hu, L. Kienle, Y.-G. Guo, J. Maier, *Adv. Mater.* **2006**, *18*, 1421.
[12] G. Armstrong, A. R. Armstrong, P. G. Bruce, P. Reale, B. Scrosati, *Adv. Mater.* **2006**, *18*, 2597.
[13] A. R. Armstrong, G. Armstrong, J. Canales, P. G. Bruce, *Angew. Chem.* **2004**, *116*, 2336; *Angew. Chem. Int. Ed.* **2004**, *43*, 2286.
[14] W. J. H. Borghols, D. Lutzenkirchen-Hecht, U. Haake, W. Chan, U. Lafont, E. M. Keider, E. R. H. van Eck, A. P. M. Kentgens, F. M. Mulder, M. Wagemaker, *J. Electrochem. Soc.* **2010**, *157*, A582.
[15] Y.-M. Lin, P. R. Abel, D. W. Flaherty, J. Wu, K. J. Stevenson, A. Heller, C. B. Mullins, *J. Phys. Chem. C* **2011**, *115*, 2585.
[16] L. J. Fu, H. P. Zhang, C. Li, T. Zhang, Y. P. Wu, H. Q. Wu, *J. Power Sources* **2006**, *159*, 219.
[17] S. Yoon, B. H. Ka, C. Lee, M. Park, S. M. Oh, *Electrochem. Solid-State Lett.* **2009**, *12*, A28.
[18] Z. Yang, G. Du, Z. Guo, X. Yu, Z. Chen, T. Guo, H. Liu, *J. Mater. Chem.* **2011**, *21*, 8591.
[19] T. Yu, Y. Deng, L. Wang, R. Liu, L. Zhang, B. Tu, D. Zhao, *Adv. Mater.* **2007**, *19*, 2301.
[20] B. Tian, X. Liu, B. Tu, C. Yu, J. Fan, L. Wang, S. Xie, G. D. Stucky, D. Zhao, *Nat. Mater.* **2003**, *2*, 159.
[21] X. Qian, Y. Wan, Y. Wen, N. Jia, H. Li, D. Zhao, *J. Colloid Interface Sci.* **2008**, *328*, 367.
[22] J. Lee, M. C. Orilall, S. C. Warren, M. Kamperman, F. J. Disalvo, U. Wiesner, *Nat. Mater.* **2008**, *7*, 222.
[23] R. Liu, Y. Ren, Y. Shi, F. Zhang, L. Zhang, B. Tu, D. Zhao, *Chem. Mater.* **2008**, *20*, 1140 – 1146.
[24] M. Oku, H. Matsuta, K. Wagatsuma, Y. Wasedab, S. Kohikic, *J. Electron Spectrosc.* **1999**, *105*, 211.
[25] H. Q. Li, R.-L. Liu, D. Zhao, Y.-Y. Xia, *Carbon* **2007**, *45*, 2628.
[26] C. Daniel, J. O. Besenhard, *Handbook of Battery Materials*, Wiley-VCH, Weinheim, **1998**, p. 384.
[27] The volumetric capacity of MACT3 was calculated from a discharge capacity of 350 $mAh\,g^{-1}$ and a theoretical density of 2.04 $g\,cm^{-3}$, which was calculated by using a measured pore volume of 0.05 $cm^3\,g^{-1}$, a TiO_2 density of 4 $g\,cm^{-3}$, a carbon density of 1.5 $g\,cm^{-3}$, and their weight fractions.
[28] The energy density was estimated by multiplication of the reversible capacity (C_{rev}) with cell voltage (V_{cell}) without considering the cathode weight. V_{cell} was obtained by extraction of the cathode voltage ($V_{cathode}$) with the anode one (V_{anode}). When $V_{cathode}$ is 4 V, the V_{cell} values of conventional TiO_2, MACT3, and graphite are assumed to be 2.5, 3.5, and 4.0 V, respectively. C_{rev} values of typical a TiO_2 anode, MACT3, and graphite are 250, 430, and 350 $mAh\,g^{-1}$, respectively.
[29] A. J. Bard, L. R. Faulkner, *Electrochemical Methods: Fundamentals and Applications*, Wiley, New York, **1988**, Chap. 9.
[30] S. Yoon, H. Kim, S. M. Oh, *J. Power Sources* **2001**, *94*, 68.
[31] F. Joho, P. Novak, M. E. Spahr, *J. Electrochem. Soc.* **2002**, *149*, A1020.
[32] M. G. Choi, Y.-G. Lee, S.-W. Song, K. M. Kim, *Electrochim. Acta* **2010**, *55*, 5975.
[33] A. V. Churikov, A. V. Ivanishev, *Electrochim. Acta* **2003**, *48*, 3677 – 3691.
[34] Y. Zhou, C. Jo, J. Lee, C. W. Lee, G. Gao, S. Yoon, *Microporous Mesoporous Mater.* **2012**, *151*, 172.
[35] T. Kemmitt, N. I. Al-Salim, G. J. Gainsford, A. Bubendorfer, M. Waterland, *Inorg. Chem.* **2004**, *43*, 6300.
[36] Y. Ishii, Y. Kanamori, T. Kawashita, I. Mukhopadhyay, S. Kawasaki, *J. Phys. Chem. Solids* **2010**, *71*, 511.
[37] R. Liu, Y. Shi, Y. Wan, Y. Meng, F. Zhang, D. Gu, Z. Chen, B. Tu, D. Zhao, *J. Am. Chem. Soc.* **2006**, *128*, 11652.
[38] L. Patterson, *Phys. Rev.* **1939**, *56*, 978.
[39] H. Zhou, S. Zhu, M. Hibino, I. Honma, M. Ichihara, *Adv. Mater.* **2003**, *15*, 2107.

Received: June 29, 2012
Published online on October 25, 2012

